

Time-resolved turbulent dynamo in a laser plasma

Archie FA Bott^{a,b,1}, Petros Tzeferacos^{a,c,d,e}, Laura Chen^a, Charlotte AJ Palmer^{a,f}, Alexandra Rigby^a, Anthony R Bell^a, Robert Bingham^{g,h}, Andrew Birkeⁱ, Carlo Graziani^j, Dustin H Froula^e, Joseph Katz^e, Michel Koenig^{k,1}, Matthew W Kunz^b, Chikang Liⁱ, Jena Meinecke^a, Francesco Miniati^a, Richard Petrassoⁱ, Hye-Sook Park^m, Bruce A Remington^m, Brian Revilleⁿ, J Steven Ross^m, Dongsu Ryu^o, Dmitri Ryutov^m, Fredrick Séguinⁱ, Thomas G White^p, Alexander A Schekochihin^a, Donald Q Lamb^c, and Gianluca Gregori^{a,c}

^aDepartment of Physics, University of Oxford, Parks Road, Oxford OX1 3PU, UK; ^bDepartment of Astrophysical Sciences, Princeton University, 4 Ivy Ln, Princeton, NJ 08544, USA; ^cDepartment of Astronomy and Astrophysics, University of Chicago, 5640 S. Ellis Ave, Chicago, IL 60637, USA; ^dDepartment of Physics and Astronomy, University of Rochester, 206 Bausch & Lomb Hall, Rochester, NY 14627; ^eLaboratory for Laser Energetics, University of Rochester, 250 E River Rd, Rochester, NY 14623, USA; ^fSchool of Mathematics and Physics, Queens University Belfast, Belfast BT7 1NN, UK; ^gRutherford Appleton Laboratory, Chilton, Didcot OX11 0QX, UK; ^hDepartment of Physics, University of Strathclyde, Glasgow G4 0NG, UK; ⁱMassachusetts Institute of Technology, 77 Massachusetts Ave, Cambridge, MA 02139, USA; ^jArgonne National Laboratory, Mathematics and Computer Science Division, Argonne, IL, USA; ^kLULI, CNRS, CEA, Ecole Polytechnique, UPMC, Univ Paris 06: Sorbonne Universités, Institut Polytechnique de Paris, F-91128 Palaiseau cedex, France; ^lGraduate School of Engineering, Osaka University, Suita, Osaka 565-0871, Japan; ^mLawrence Livermore National Laboratory, 7000 East Ave, Livermore, CA 94550, USA; ⁿMax-Planck-Institut für Kernphysik, Postfach 10 39 80, 69029 Heidelberg, Germany; ^oDepartment of Physics, School of Natural Sciences, UNIST, Ulsan 44919, Korea; ^pDepartment of Physics, University of Nevada, Reno, Nevada 89557, USA

This manuscript was compiled on February 17, 2021

1 Understanding magnetic-field generation and amplification in turbu-
2 lent plasma is essential to account for observations of magnetic
3 fields in the universe. A theoretical framework attributing the ori-
4 gin and sustainment of these fields to the so-called fluctuation dy-
5 namo was recently validated by experiments on laser facilities in low-
6 magnetic-Prandtl-number plasmas ($P_m < 1$). However, the same
7 framework proposes that the fluctuation dynamo should operate dif-
8 ferently when $P_m \gtrsim 1$, the regime relevant to many astrophysical en-
9 vironments such as the intracluster medium of galaxy clusters. This
10 paper reports a new experiment that creates a laboratory $P_m \gtrsim 1$
11 plasma dynamo for the first time. We provide a time-resolved charac-
12 terization of the plasma's evolution, measuring temperatures, densi-
13 ties, flow velocities and magnetic fields, which allows us to explore
14 various stages of the fluctuation dynamo's operation on seed mag-
15 netic fields generated by the action of the Biermann-battery mecha-
16 nism during the initial drive-laser target interaction. The magnetic
17 energy in structures with characteristic scales close to the driving
18 scale of the stochastic motions is found to increase by almost three
19 orders of magnitude and saturate dynamically. It is shown that the
20 initial growth of these fields occurs at a much greater rate than the
21 turnover rate of the driving-scale stochastic motions. Our results
22 point to the possibility that plasma turbulence produced by strong
23 shear can generate fields more efficiently at the driving scale than
24 anticipated by idealized MHD simulations of the nonhelical fluctua-
25 tion dynamo; this finding could help explain the large-scale fields
26 inferred from observations of astrophysical systems.

Magnetic fields | Fluctuation dynamo | Laboratory astrophysics |

1 Cosmic magnetic fields play a dynamically important role
2 in a myriad of astrophysical environments (1, 2). Under-
3 standing how these fields attained such strengths is a long-
4 standing question in astrophysics (3). Most physical processes
5 thought to generate seed magnetic fields in initially unmagne-
6 tized plasma, such as the Biermann battery mechanism (4),
7 predict field-strength values in astrophysical settings that are
8 far smaller than those observed (5, 6), necessitating the exist-
9 ence of some mechanism for amplifying fields and maintaining
10 them at their observed magnitudes (7, 8). One possible mecha-
11 nism is the fluctuation dynamo, whereby stochastic motions of
12 plasma lead to stretching, twisting and folding of magnetic-field
13 lines (9, 10). In this dynamo, fields are amplified exponentially
14 until their strength comes into approximate equipartition with
15 the fluid kinetic energy, saturating growth.

The fluctuation dynamo is best understood in the context
of resistive magnetohydrodynamics (MHD) thanks to both
analytical calculations (11–14) and simulations (15–25). In
resistive MHD, the fluctuation dynamo can only operate if
the magnetic Reynolds number $R_m \equiv u_L L / \eta$ – where L is the
length scale of driving stochastic motions, u_ℓ the characteristic
velocity of motions at a given scale ℓ , and η the resistivity
of the plasma – is above some critical threshold, $R_{m,c}$ (26).
The precise value of this threshold depends on the magnetic
Prandtl number P_m of the plasma (21, 27, 28), defined by
 $P_m \equiv R_m / Re = \nu / \eta$ (where $Re \equiv u_L L / \nu$ is the fluid Reynolds
number and ν is the kinematic viscosity), as well as the Mach
number and driving mechanism of the stochastic motions (29).
If this threshold is surpassed, then any initially dynamically
insignificant magnetic field is amplified, and most rapidly so
near the resistive scale $\ell_\eta \ll L$ (for $P_m \ll 1$, $\ell_\eta \sim \eta / u_{\ell_\eta}$; for
 $P_m \gtrsim 1$, $\ell_\eta \sim \eta / u_{\ell_\nu}$). The nature of this amplification depends

Significance Statement

Our laser-plasma experiment has reproduced the physical process thought to be responsible for generating and sustaining magnetic fields in turbulent plasmas (the ‘fluctuation dynamo’), and, for the first time in the laboratory, has accessed the viscosity-dominated regime of relevance to most of the plasma in the universe. Also for the first time, these measurements are time-resolved, which provides evolutionary information about the fluctuation dynamo (including the field’s growth rate) previously only available from simulations. The efficient amplification of large-scale magnetic fields seen in our experiment could explain the origin of large-scale fields that are observed in turbulent astrophysical plasmas, but are not predicted by current analytical calculations or idealized simulations of the fluctuation dynamo.

This project was conceived by G.G., D.Q.L., P.T., A.F.A.B., and A.A.S. The delivery of the experiment was led by G.G. and L.C. A.B., C.-K.L. and R.P. contributed to the proton radiography development and data extraction, while D.H.F. and J.K. contributed to the Thomson scattering diagnostics. P.T. designed, executed, and analyzed the FLASH simulations. The analysis of the experimental and simulation data was led by A.F.A.B. with support from P.T., L.C., C.P., A.R., A.R.B., R.B., A.B., C.G., J.K., M.K., C.-K.L., J.M., J.M., R.P., H.-S.P., B.A.R., B.R., J.S.R., D.Ryu, D.Ryutov, T.G.W., A.A.S., D.Q.L., and G.G. The paper was written by A.F.A.B. with contributions from all other co-authors.

The authors declare that they have no conflicts of interest.

¹To whom correspondence should be addressed. E-mail: abott@princeton.edu

33 on Pm, because Pm determines the relative magnitudes of ℓ_η
 34 and the viscous scale $\ell_\nu \sim \nu/u_{\ell_\nu}$, and thereby whether the
 35 stochastic fluid motions driving dynamo action are smooth or
 36 chaotic (27). The $\text{Pm} \ll 1$ regime is relevant to stellar and
 37 planetary dynamos, while the $\text{Pm} \gtrsim 1$ regime is pertinent to
 38 hot, diffuse plasmas such as many astrophysical disks or the
 39 intracuster medium (ICM) (10).

40 A fundamental question about the character of the fluctuation
 41 dynamo in resistive MHD concerns the rate of magnetic-
 42 field growth at a given scale. When the growing field is
 43 dynamically insignificant, its spectrum is peaked near the
 44 resistive scale (11, 14); magnetic fluctuations at this scale
 45 grow exponentially, at a rate proportional to the character-
 46 istic turnover rate $\gamma_{\ell_\nu} \sim u_{\ell_\nu}/\ell_\nu$ of motions at the viscous
 47 scale (for $\text{Pm} \gtrsim 1$). For Kolmogorov turbulence, γ_{ℓ_ν} greatly
 48 exceeds the characteristic turnover rate $\gamma_L \sim u_L/L$ of the
 49 driving-scale stochastic motions. Once the magnetic energy at
 50 resistive scales becomes comparable to the kinetic energy at
 51 the viscous scale, MHD simulations indicate that the magnetic-
 52 energy spectrum changes, with the total energy continuing to
 53 grow – albeit secularly rather than exponentially – and the
 54 peak wavenumber moving to scales larger than the resistive
 55 scale (19, 23, 30). Whether the peak wavenumber ultimately
 56 moves to the driving scale of the motions depends on Pm:
 57 previous simulations of the $\text{Pm} \sim 1$ dynamo (with non-helical
 58 flow) suggest that in the saturated state of the dynamo the
 59 peak wavenumber is a factor of a few larger than the driving
 60 wavenumber (22, 31), while for $\text{Pm} \gg 1$, an excess of energy
 61 remains near the resistive scale (19). Thus, whilst simulations
 62 of the fluctuation dynamo show that magnetic fields can be
 63 amplified very quickly at the resistive scale, dynamically sig-
 64 nificant fields on the driving scales only develop after many
 65 driving-scale eddy turnover times, or possibly not at all.

66 With dynamo experiments now possible, we have a method
 67 for exploring both the requirements for, and the properties
 68 of, the fluctuation dynamo. Until recently, experimental in-
 69 vestigations of plasma dynamos were limited by the practical
 70 difficulty of realizing sufficiently large values of Rm in the
 71 laboratory (32–35). However, a recent laser-plasma experi-
 72 ment (36, 37) carried out on the Omega Laser Facility (38)
 73 demonstrated the feasibility of the fluctuation dynamo in a
 74 turbulent plasma at $\text{Pm} < 0.5$. In that experiment, a region
 75 of turbulent plasma was created by colliding two laser-plasma
 76 jets that had first passed through offset grids. The state of
 77 this region was characterized, and the magnetic Reynolds
 78 number $\text{Rm} \approx 600$ was above the necessary threshold for the
 79 onset of the fluctuation dynamo in MHD. Magnetic fields were
 80 measured using both polarimetry and proton imaging, and
 81 the magnetic-energy density in the turbulent plasma a few
 82 turnover times after collision was found to be several orders
 83 of magnitude larger than that present during the turbulent
 84 region’s formation. Most significantly, this magnetic-energy
 85 density was a finite fraction of the turbulent kinetic-energy
 86 density, a key signature of the saturated fluctuation dynamo.

87 In this paper, we report new experiments on the Omega
 88 Laser Facility, which employs a re-designed version of the plat-
 89 form described in (37) to create the first laboratory $\text{Pm} \gtrsim 1$
 90 fluctuation dynamo. As before, we used three-dimensional
 91 radiation-MHD simulations with FLASH (39, 40) to design
 92 and interpret the experiments – see Supplementary Informa-
 93 tion for details. Also for the first time, by carrying out multiple

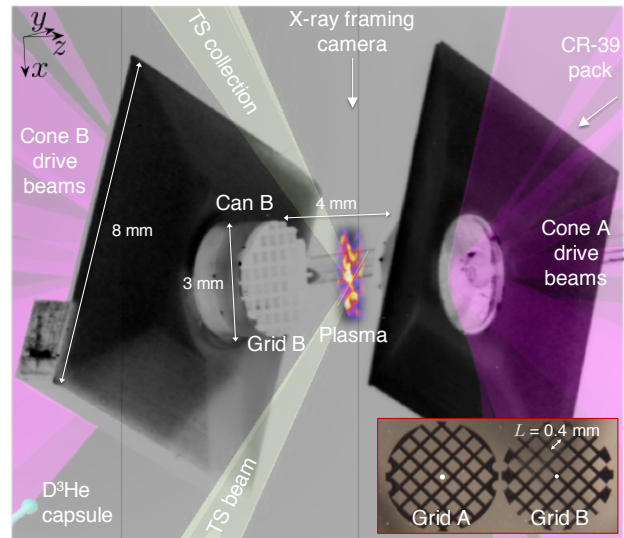


Fig. 1. Experimental set-up. An annotated photograph of a target used in our experiment. The laser-beam-driven foils are composed of CH plastic (i.e., 50% carbon, 50% hydrogen by atom number) and are 3 mm in diameter and 50 μm in thickness; attached to the front sides of each foil are 230 μm thick, 3 mm diameter annular ‘washers’, also composed of CH plastic, with a 400 μm central hole. The separation between the two opposing foils is 8 mm. The shields (which prevent direct interaction between the front- and rear-side blow-off plasmas) are also CH plastic. CH plastic cans attach polyimide grids to the foils; the grids themselves are 250 μm thick, with a 3 mm diameter, 300 μm holes and 100 μm wires. The holes in the opposing grids are chosen to be offset (see bottom right); grid A has a hole located at its center, while grid B has crossing rods. Ten 500 J drive beams (individual pulse length 1 ns) with 351 nm wavelength and 800 μm focal spot size were applied to each foil, configured to deliver a 10 ns staggered flat pulse shape with a total energy per foil of 5 kJ. The orientation of the Thomson scattering (TS) beam is denoted, as well as the cylindrical scattering volume and collection direction. A D^3He capsule is attached to the target for the proton imaging diagnostic (see Materials and Methods for details): fusion protons are generated by the capsule’s implosion, pass between the target grids, and are detected via a CR-39 pack positioned as shown. For ease of reference between figures, we have defined an (x, y, z) Cartesian coordinate system with axes as shown, whose origin is at the target’s center.

identical experiments, we are able to provide a time-resolved
 characterization of this plasma dynamo’s evolution by measur-
 ing spatially averaged electron and ion temperatures, densities,
 flow velocities, and magnetic fields with a time resolution
 smaller than the turnover time of the plasma’s driving-scale
 stochastic motions. Such a characterization is an important
 advance over our previous OMEGA experiment, which did
 not measure the growth rate of magnetic fields. Finally, the
 concerted analysis of the experimental data in tandem with
 the simulation results enabled a thorough assessment of the
 dynamo mechanism realized in our experiment.

Experimental Design

The experimental platform employed for the experiment (see
 Fig. 1 for a schematic of the experimental target) gener-
 ates a turbulent plasma in the following manner. Ten long-
 pulse laser beams illuminate two opposing CH foils, creating
 counter-propagating supersonic plasma jets. These jets then
 pass through offset grids before colliding at the experimen-
 tal target’s center. On collision, the jets coalesce, forming
 an ‘interaction region’ of plasma (demarcated by two shocks)
 whose density and temperature are significantly greater than
 that of either jet. The inhomogeneity and asymmetry of the

116 initial plasma-jet density and flow profiles gives rise to signifi-
 117 cant shearing motions in the interaction region; this facilitates
 118 Kelvin-Helmholtz (KH) instabilities over a range of length
 119 scales, and thus significant stochasticity emerges in the flow
 120 profile as the interaction region develops. In contrast to the
 121 initial jet motion, stochastic motions in the interaction region
 122 are subsonic, because of their reduced characteristic speeds
 123 and the higher temperature of the plasma in the interaction-
 124 region (a result of compressive heating). At a given instant, we
 125 characterize this plasma using various experimental diagnos-
 126 tics: X-ray imaging for investigating the spatial distribution
 127 of the plasma in the interaction region plasma (see Section A),
 128 optical Thomson scattering for measuring the plasma proper-
 129 ties (Section B), and proton imaging for quantifying magnetic
 130 fields (Section C).

131 Despite some similarities with the previous OMEGA exper-
 132 iment investigating dynamo processes (37), the design of
 133 the new experiment was different in a key regard. In order to
 134 realize a larger Pm, chlorine dopants previously introduced
 135 into the CH foils to enhance X-ray emissivity of the plasma
 136 were removed. Their presence in even moderate quantities was
 137 found to reduce initial plasma-jet velocities, cool the plasma
 138 radiatively and increase the effective ion charge; all three ef-
 139 fects in combination reduced Pm significantly. We also made
 140 a number of other improvements to the target's design. The
 141 thickness of the grid wires was decreased to 100 μm , whilst
 142 the hole width was kept at 300 μm (see Fig. 1, bottom right).
 143 This change was made in order to deliver more kinetic energy
 144 to the interaction region and reduce the inhomogeneity of the
 145 interaction region's global morphology arising from the asym-
 146 metry of the grids. Finally, rod supports connecting the grids
 147 to the CH foils were removed and the grids instead attached
 148 via CH 'cans' (see Fig. 1). This alteration provided both the
 149 X-ray framing camera and proton imaging diagnostics with un-
 150 obstructed views of the interaction region. Further discussion
 151 of these target modifications is given in (41).

152 We also changed somewhat our methodology for diagnosing
 153 the plasma state. Instead of employing the Thomson-scatter-
 154 ing diagnostic to measure polarization [as was done in (37)],
 155 we used it to measure the spectra of high-frequency fluctua-
 156 tions [the electron-plasma-wave (EPW) feature] as well as
 157 low-frequency fluctuations [the ion-acoustic-wave (IAW) fea-
 158 ture] concurrently. Furthermore, instead of the previous setup
 159 that measured the scattering spectrum in a small volume dur-
 160 ing a 1-ns time window, we employed a spatially resolved, 1-ns
 161 time-integrated set-up that measured the plasma parameters in
 162 a cylindrical region passing through the grids' midpoint, with
 163 length 1.5 mm and a 50 μm^2 cross-sectional area (see Fig. 1).
 164 This enabled us to measure simultaneously the values of a
 165 number of plasma parameters characterizing the interaction-
 166 region plasma: mean electron number density \bar{n}_e , fluctuating
 167 electron number density Δn_e , electron temperature T_e , ion
 168 temperature T_i , inflow velocity \bar{u}_{in} and small-scale stochastic
 169 velocity Δu . Removing polarimetry from this experiment did
 170 not inhibit our ability to measure magnetic fields, because we
 171 had previously validated the accuracy of such measurements
 172 obtained using proton imaging (42).

173 In order to characterize the growth of the magnetic fields in
 174 our experiment with the requisite time resolution, we began to
 175 collect data prior to collision and continued to do so at 1.5-ns
 176 intervals (on different experimental shots). This time interval

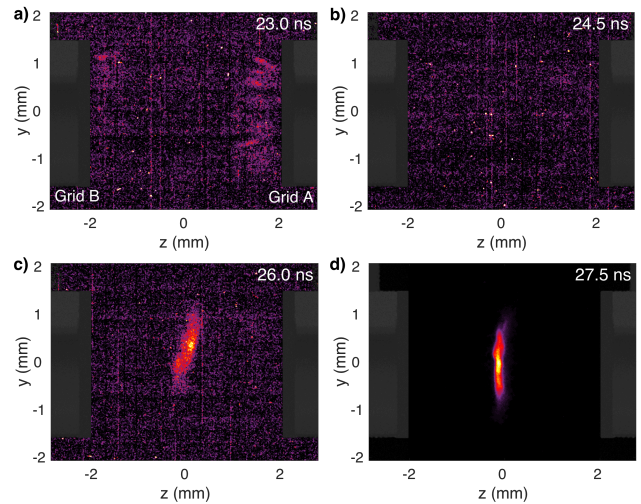


Fig. 2. X-ray self-emission prior to and at formation of the interaction region. The featured sequence of X-ray images are taken on different experimental shots. The first three images are adjusted to have the same color map, normalized to the maximum pixel count (56 counts) of c); the final image is normalized to its own maximum pixel count. We note that the absence of noise in d) is due to the much higher signal-to-noise ratio. To aid interpretation of the images, a projection of the target is superimposed in dark gray on each image. The respective timings (in ns) of the images after drive-beam laser-pulse initiation are **a)** 23.0 ns, **b)** 24.5 ns, **c)** 26.0 ns, and **d)** 27.5 ns.

177 was correctly anticipated to be less than half of the turnover
 178 time of driving-scale eddies (~ 4 ns), based on FLASH simula-
 179 tions that were validated by our earlier experiment (36, 37).
 180 Detailed specifications of the X-ray framing camera diagnostic,
 181 the Thomson-scattering diagnostic and the proton-imaging
 182 diagnostic are given in Materials and Methods.

183 Measurements

A. Measuring turbulence: self-emission X-ray imaging. With
 184 the fixed X-ray framing camera's bias employed in our exper-
 185 iment (see Materials and Methods), we find that for times
 186 $\lesssim 25$ ns, self-emitted X-rays from the individual plasma jets
 187 are barely detectable (see Fig. 2a and Fig. 2b). However,
 188 around 26 ns after the onset of the driving laser pulses, a
 189 region of emission situated approximately halfway between
 190 the grids emerges (Fig. 2c). 1.5 ns later, the total intensity of
 191 the region is significantly higher (Fig. 2d). We conclude that
 192 the two plasma flows collide and form the interaction region at
 193 around 26 ns. Subsequent to the formation of the interaction
 194 region, the size of the region of bright emission increases both
 195 in the direction parallel to the 'line of centers' (that is, to
 196 the line connecting the midpoints of grid A and grid B) and
 197 perpendicular to it (see Fig. 3). Emission peaks 3 ns after
 198 the interaction-region's coalescence, before decaying away at
 199 later times (first column of Fig. 3). Random fluctuations in
 200 the detected X-ray intensity across the emitting region appear
 201 concurrently with the peak emission (second column, Fig. 3)
 202 and subsequently become clearly noticeable by eye.
 203

204 In order to distinguish fluctuations in emission from global
 205 inhomogeneities in the total self-emission from the interaction-
 206 region plasma, we construct relative X-ray intensity maps
 207 based on experimentally derived mean emission profiles (a
 208 technical description of how these profiles are derived is given in
 209 the Supplementary Information). The mean emission profiles

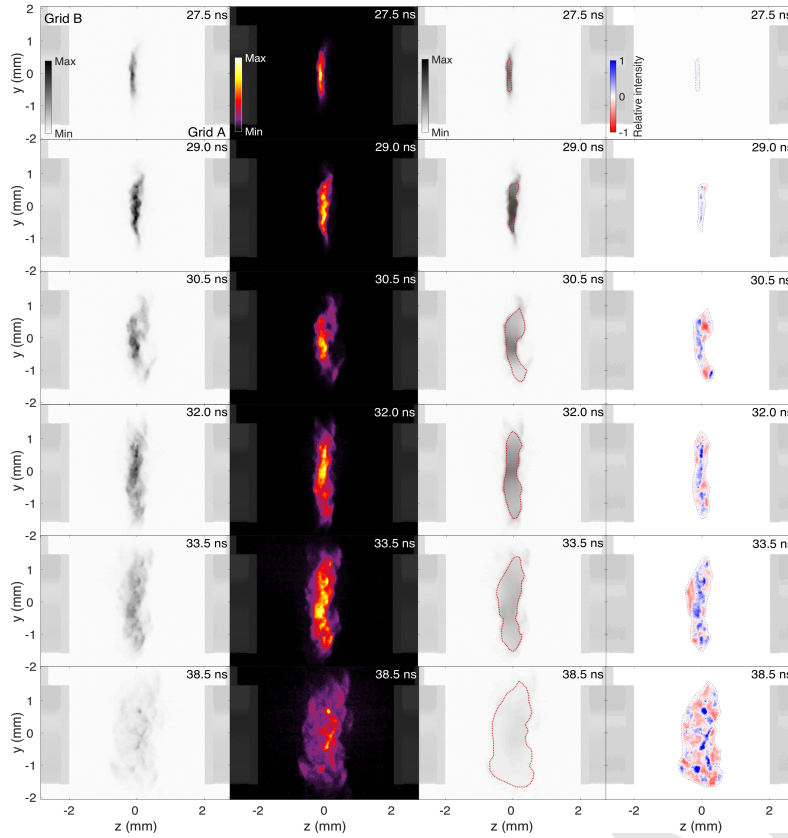


Fig. 3. The interaction-region plasma's evolution. Self-emission X-ray images of the interaction-region plasma. Each image was recorded at the indicated time in a different experimental shot. First column: absolute X-ray intensity images, normalized to a maximum count value of 1,050 (the maximum count value associated with the interaction-region plasma in any of the images). Second column: X-ray intensity images normalized by the maximum pixel value in the image. Third column: mean emission profiles calculated from the far-left column; the boundary denoted in red in each image is that used to calculate the two-dimensional (2D) Gaussian window function discussed in the main text and the gray-scale map is the same as in the far-left images. Fourth column: relative X-ray intensity map calculated from the mean emission profile. Fluctuations with a positive value with respect to the mean intensity are denoted in blue, negative in red, with maximum and minimum values set at $\pm 100\%$ of the mean value. Self-emission images for the FLASH simulations, as well as mean emission profiles and relative X-ray intensity maps associated with those images, are shown in Fig. S15 of the Supplementary Information.

calculated for the X-ray images shown in the first column of Fig. 3 are given in the third column of the same figure and the corresponding relative-intensity images are presented in the fourth column.

Quantitative analysis of the X-ray images can be carried out by noting that the plasma jets are fully ionized even prior to collision ($T_e \approx 180$ eV), and so X-ray emission from the plasma during the interaction is dominated by free-free bremsstrahlung. Assuming a thermal distribution of particles, the bremsstrahlung spectral density $\epsilon_{\omega}^{\text{ff}}$ for a CH plasma is given by (43)

$$\epsilon_{\omega}^{\text{ff}} = 1.1 \times 10^{-38} Z_{\text{eff}} n_e^2 T_e^{-1/2} \exp\left(-\frac{\hbar\omega}{k_B T_e}\right) \bar{g}_{\text{ff}} \text{ erg cm}^{-3}, \quad [1]$$

where $Z_{\text{eff}} = (Z_C^2 + Z_H^2)/(Z_C + Z_H)$ is the effective ion charge seen by electrons (Z_H and Z_C being the charges of hydrogen and carbon ions, respectively), ω the frequency of radiation, k_B Boltzmann's constant, and \bar{g}_{ff} the velocity-averaged Gaunt factor. Since the interaction-region plasma is optically thin to X-rays detected by the framing camera, the measured (optical) intensity I on the CCD camera satisfies $I \propto \int ds \int d\omega \epsilon_{\omega}^{\text{ff}} \hat{R}(\omega)$, where the integral is performed along the line of sight, and $\hat{R}(\omega)$ is a function incorporating the (relative) frequency-dependent responses of both the X-ray camera filter and the microchannel plate (MCP) (see Supplementary Information, Fig. S1). Substituting Eq. [1] into this proportionality relation, we find $I = I(n_e, T_e) \propto \int ds n_e^2 \hat{f}(T_e)$, where

$$\hat{f}(T_e) = \frac{\hat{A}}{T_e^{-1/2}} \int d\omega \hat{R}(\omega) \exp\left(-\frac{\hbar\omega}{k_B T_e}\right), \quad [2]$$

and \hat{A} is a normalization constant. The function $\hat{f}(T_e)$ is plotted in the Supplementary Information (Fig. S1b); its key property is that for temperatures ~ 300 –500 eV (the characteristic temperature of the plasma just after interaction-region formation – see Section B), the measured X-ray intensity is only weakly dependent on temperature. However, the X-ray intensity is a sensitive function of the electron number density: in short, our X-ray images essentially provide electron-density measurements.

This conclusion is significant for several reasons. First, the full-width-half-maximum (FWHM) of the emitting region can be used as a reasonable measure of the width l_n of the interaction region, on account of its increased density compared to either jet. Determining this width is essential for extracting magnetic-field estimates from the proton-imaging diagnostic (see Section C). Fig. 4a illustrates how this measurement is carried out in practice: we consider three vertically averaged lineouts of the mean emission profile, calculate the FWHMs of these lineouts, and then estimate the error of the measurement from the standard error of the FWHMs. The mean emission profile is marginally more robust than the original X-ray image for calculating l_n because fluctuations distort the measured maximum value of the vertically averaged profile. The resulting values of l_n are shown in Fig. 4c, in blue. Following an initial decrease in value immediately after the two plasma flows collide to form the interaction region, l_n increases steadily over time.

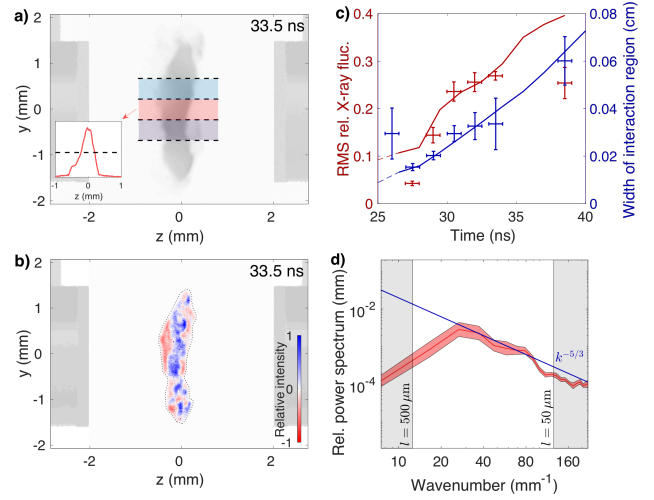
Secondly, relative fluctuations δI in X-ray intensity (such as those shown in Fig. 4b) are closely correlated with fluctuations δn_e of electron density; indeed, for intensity fluctuations that are small compared to the mean intensity \bar{I} , $\delta I/\bar{I} \approx 2/l_{n\perp} \int ds \delta n_e/\bar{n}_e$, where $l_{n\perp}$ is the perpendicular

267 extent of the interaction region (and we have assumed that
 268 $\delta T_e/\bar{T}_e \lesssim \delta n_e/\bar{n}_e$, which is justified by the small Péclet number
 269 of the interaction-region plasma: $Pe \approx 0.2$). The root-
 270 mean-square (RMS) of the relative X-ray fluctuations therefore
 271 provides a simple measure of the onset of stochasticity in the
 272 interaction region. The increase in relative X-ray fluctuation
 273 magnitude $(\delta I/\bar{I})_{\text{rms}}$ shown in Fig. 4c (in red) illustrates
 274 that significant fluctuations develop in a 5-ns interval fol-
 275 lowing formation of the interaction region, after which their
 276 magnitude saturates at a finite fraction of the mean X-ray
 277 intensity of the region: $\delta I \lesssim 0.3\bar{I}$. Under the additional as-
 278 sumption that density fluctuations are statistically isotropic
 279 and homogeneous (see Fig. S16 for a justification of this),
 280 and therefore contribute to the line-of-sight integral as a
 281 random walk provided many fluctuations are sampled, we
 282 find $\delta n_e/\bar{n}_e \lesssim (l_{n\perp}/L_{\text{int},n})^{1/2} \delta I/2\bar{I}$, where $L_{\text{int},n}$ is the inte-
 283 gral scale of the density fluctuations in the plasma. Taking
 284 $l_{n\perp} \lesssim 0.3$ cm and $L_{\text{int},n} \approx L \approx 0.04$ cm (corresponding to
 285 the grid periodicity), we deduce that $\delta n_e/\bar{n}_e \lesssim 0.5$. Thus, it
 286 follows that density fluctuations are not large compared to the
 287 mean density and thus the stochastic motions of the plasma
 288 are subsonic.

289 Thirdly, under the same statistical assumptions, the power
 290 spectrum of the path-integrated density fluctuations derived
 291 from the X-ray intensity fluctuations can be directly related to
 292 the power spectrum of the density fluctuations (44). Because
 293 fluctuating density in a subsonic plasma behaves as a passive
 294 scalar (45), this in turn allows for the measurement of the
 295 velocity power spectrum (37). The result of such a calcula-
 296 tion applied to Fig. 4b is shown in Fig. 4d: the spectrum
 297 extends across the full range of resolved wavenumbers and,
 298 for characteristic wavenumbers $2\pi/L \lesssim k < k_{\text{res}} = 127 \text{ mm}^{-1}$,
 299 the spectral slope is consistent with the Kolmogorov power
 300 law, as expected for a turbulent, subsonic plasma (46).

301 **B. Measuring plasma parameters: Thomson-scattering diag-**
 302 **nostic.** For experimental times approximately coincidental
 303 with the collision of the two plasma flows, and just after,
 304 clear scattering spectra at both low and high frequencies were
 305 obtained. Unprocessed IAW and EPW features for a sample
 306 time close to the formation of the interaction region are shown
 307 in Figs. 5a and 5b, respectively; the complete data set used
 308 for these results is given in the Supplementary Information
 309 (Fig. S2). Measurements of the bulk plasma parameters listed
 310 in Experimental Design were then derived at a given position
 311 by fitting the spectral density function (see Materials and
 312 Methods). We averaged the parameters obtained from fits at
 313 each position over the complete spatial extent of the observed
 314 IAW and EPW features. The time evolution of the physical
 315 parameters was obtained by repeating the experiment and
 316 firing the Thomson-scattering diagnostic at different times
 317 with respect to the activation of the drive-beam.

318 The evolution of the average electron and ion temperatures
 319 in the Thomson-scattering volume is shown in Fig. 5c, density
 320 in Fig. 5d, and bulk and turbulent velocities in Fig. 5e.
 321 At 24 ns, the characteristic electron and ion temperatures
 322 were $T_e \approx T_i \approx 180 \text{ eV}$, the characteristic flow speed $\bar{u}_{\text{in}} \approx$
 323 260 km s^{-1} , and the mean electron number density $\bar{n}_e \approx$
 324 $2.5 \times 10^{19} \text{ cm}^{-3}$. These values are similar to those previously
 325 obtained for a single plasma jet (37), a finding consistent with
 326 the observation from the X-ray imaging diagnostic that the
 327 two plasma flows have not yet collided to form the interaction-



301 **Fig. 4. Characterizing the interaction-region plasma using X-ray imaging. a)**
 302 Mean emission profile of an X-ray image, recorded 33.5 ns after drive-beam pulse
 303 initiation, shown with regions used to calculate average one-dimensional (1D) parallel
 304 profiles. One such profile, along with the half-maximum value, is also depicted.
 305 **b)** Relative X-ray intensity map associated with mean emission profile given in a).
 306 **c)** Root-mean-square (RMS) of relative X-ray fluctuations (in red) and the width of
 307 the interaction region l_n over time (in blue). The behavior of both quantities
 308 in the FLASH simulations is also shown (red/blue curves). The dashed portion of
 309 the curves correspond to times when the interaction-region plasma is not yet fully
 310 collisional and so the simulations are not yet formally valid (see Supplementary
 311 Information). To determine an error of the RMS fluctuation measurement, the RMS
 312 values of fluctuations in images recorded at the same time are employed. **d)** 1D
 313 power spectrum of the relative density fluctuations (red line), calculated from the
 314 relative X-ray intensity map given in b). The error on the spectrum (pink patch) is
 315 determined using the power spectrum of b) and the power spectrum of the relative
 316 X-ray intensity map derived from the perturbed X-ray image at 33.5 ns equivalent to
 317 b) (cf. Fig. S7).

318 region plasma at this time (see Fig. 2). By contrast, 1.5 ns later the electron and ion temperatures were found to be much
 319 larger than their jet pre-collision values: $T_e \approx T_i \approx 450 \text{ eV}$.
 320 The measured mean electron number density also increased to
 321 $\bar{n}_e \approx 8 \times 10^{19} \text{ cm}^{-3}$. In fact, a range of densities were observed,
 322 with $\Delta n_e \approx 2 \times 10^{19} \text{ cm}^{-3}$, suggesting chaotic motions. For
 323 a measured characteristic sound speed of $c_s \approx 220 \text{ km s}^{-1}$,
 324 this range of densities implies small-scale stochastic velocities
 325 $\Delta u \approx 55 \text{ km s}^{-1}$ (see Materials and Methods). Assuming
 326 Kolmogorov scaling for the random small-scale motions – as
 327 is consistent with the spectrum in Fig. 4d – the characteristic
 328 velocity u_ℓ at scale ℓ satisfies $u_\ell \sim u_{\text{rms}}(\ell/L)^{1/3}$. Because the
 329 dominant contribution to Δu arises from stochastic motions
 330 with scale comparable to the Thomson scattering cross-section
 331 width $l_{\text{TS}} \approx 50 \mu\text{m}$, we conclude that $\Delta u \approx u_{l_{\text{TS}}}$, and so
 332 $u_{\text{rms}} \approx 110 \text{ km s}^{-1}$.

333 In the 3-ns interval subsequent to the two plasma flows
 334 colliding to form the interaction region, the ion temperature
 335 increased above the electron temperature ($T_i \approx 600 \text{ eV}$), before
 336 both fell to lower values ($T_e \approx T_i \approx 400 \text{ eV}$). The mean
 337 electron number density increased monotonically over the same
 338 interval, with a final measured value of $\bar{n}_e \approx 1.8 \times 10^{20} \text{ cm}^{-3}$.
 339 The relative magnitude of density fluctuations remained the
 340 same ($\Delta n_e/\bar{n}_e \approx 0.25$) over the interval.

341 At later times, no EPW feature was observed and the
 342 IAW feature manifested itself erratically (see Fig. S3 in the
 343 Supplementary Information). We believe that this was due
 344 to the increased density of the interaction region (as well as
 345 substantial density gradients) resulting in significant refraction
 346

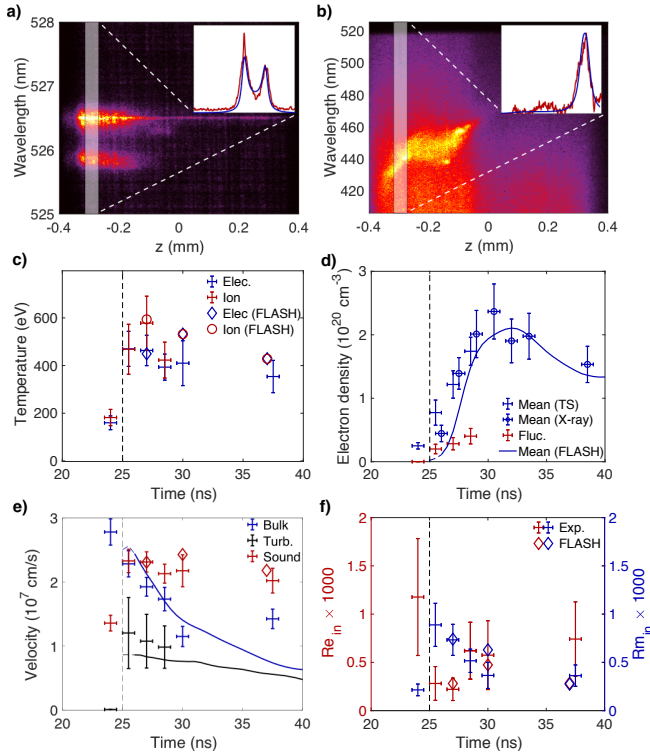


Fig. 5. Time-evolution of interaction-region plasma parameters. **a)** Low-frequency, spatially resolved spectrum (IAW feature) obtained at 27.2 ns. A sample spectral fit (for the white highlighted region) is shown in the inset. **b)** High-frequency, spatially resolved spectrum (EPW feature) and spectral fit (inset) obtained on the same shot. **c)** Evolution of electron and ion temperatures over time in the Thomson scattering volume. The experimental values for the electron (blue) and ion (red) temperatures are shown as time intervals with vertical error bars. All values are determined as described in the main text; errors for each time are determined by regarding each spatially resolved measurement as a sample of the mean temperature value for the interaction region, with the uncertainty on each sample determined by the fit sensitivity. The results of the FLASH simulations (see the Supplementary Material) for the electron temperature are shown as blue diamonds, those for the ion temperature as red circles. **d)** Evolution of mean electron density \bar{n}_e (blue) and the fluctuating density Δn_e (red) with time in the interaction region. Also shown are experimental values of \bar{n}_e derived from the self-emission X-ray images (open blue circles). The error bars are calculated in the same manner as for the temperature. The blue curve shows the results of the FLASH simulations. **e)** Evolution of bulk flow speed \bar{u}_{in} (blue), sound speed c_s (red) and turbulent velocity u_{rms} (black) with time in the Thomson-scattering volume. Errors are calculated in the same way as those for the temperature. Also shown are the results of the FLASH simulations for the bulk flow speed (blue curve), turbulent velocity (black curve), and sound speed (red diamonds). **f)** Evolution of the (bulk) fluid Reynolds number $Re_{in} \equiv \bar{u}_{in} L / \nu$ (red) and magnetic Reynolds number $Rm_{in} \equiv \bar{u}_{in} L / \eta$ (blue) over time. The kinematic viscosity ν and resistivity η are calculated using the formulae given in Table S2 of the Supplementary Information. The input plasma state variables are the experimentally-determined values in the Thomson-scattering volume and $L = 400 \mu\text{m}$; at later times (30 ns, 37.5 ns), Re_{in} is instead calculated using an extrapolated density derived from the X-ray measurements, and assuming $T_i = T_e$. Errors are calculated in the same way as those for the temperature. Also shown are the results of the FLASH simulations for Re_{in} and Rm_{in} (red/blue diamonds).

where $\bar{I}(t)$ is the mean measured intensity on the CCD at time t . Thus, assuming a reference value for $\bar{n}_e(t_2)$ at $t_2 = 29.0$ ns (derived via linear interpolation from the Thomson-scattering density measurements), we obtain the evolution profile shown in Fig. 5d. The results imply that the density continues to rise for ~ 2 ns after the final Thomson-scattering measurement of density is obtained, reaching a peak value $\bar{n}_e \approx 2.4 \times 10^{20} \text{ cm}^{-3}$ at $t = 30$ ns before falling slightly at later times.

We were still able to use the IAW feature to measure the bulk flow velocity and the electron temperature in some spatial locations at later times. The bulk flow velocity was found to drop to $\sim 100 \text{ km s}^{-1}$ at 30 ns. At 37.5 ns a similar value was obtained but with a reversed sign; this is possibly due to the Thomson-scattering diagnostic measuring the inflow velocity at a position displaced from the line of centers, which could have an opposite velocity. The electron temperature measured by the Thomson scattering diagnostic remained ~ 400 eV at later times. However, this is due to heating of the interaction region by the Thomson-scattering beam, which is significant at later times because of the high densities and reduced temperatures. We discuss this effect at greater length in the Supplementary Information with the aid of FLASH simulations.

C. Measuring magnetic fields: proton-imaging diagnostic.

The 15.0-MeV proton images for our experiment are presented as a time sequence in the top two rows of Fig. 6. The proton image before the formation of the interaction-region plasma (Fig. 6, 24.2 ns) shows little structure at the center of the grids, which is consistent with the absence of significant magnetic fields. Around the time when the interaction region forms, a moderate diminution of the proton flux is observed in a central region between the grids (Fig. 6, 25.7 ns), with characteristic magnitude Ψ similar to the mean proton flux Ψ_0 : $|\Psi - \Psi_0| \lesssim 0.3\Psi_0$. In contrast, in all subsequent proton images (beginning at $t \gtrsim 27.2$ ns), order-unity variations in the proton flux are measured ($|\Psi - \Psi_0| \gtrsim \Psi_0$) whose structure and position are (at least partially) stochastic – see Fig. 6, 27.2 ns, for an example. This is consistent with a dramatic change in the morphology and strength of the magnetic field.

Further analysis can be performed by reconstructing directly from the measured proton image the (perpendicular) path-integrated field experienced by the imaging proton beam – quantities that are related via a well-known relation (47, 48). Provided the gradients in the magnetic-field strength are not so large as to cause the proton beam to self-intersect before arriving at the detector, this relation leads to an equation of Monge-Ampère type, the unique inversion of which is a well-posed mathematical problem (49) and for which an efficient inversion algorithm exists (48) (we refer to this algorithm as the ‘field-reconstruction algorithm’). The results of applying this algorithm to the proton images shown in Fig. 6 are presented in the same figure. The strength and morphology of the reconstructed path-integrated fields after the jet collision are quite different from those at collision, with peak values reaching $\sim 8 \text{ kG cm}$ (as opposed to $\sim 1 \text{ kG cm}$ at collision) and randomly orientated filamentary structures evident.

With the path-integrated magnetic field having thus been determined, the correct method of estimating the characteristic magnetic-field strength depends on the field structure. The path-integrated field structures evident at early times (i.e., Fig. 7a) are non-stochastic. We therefore follow a standard method for analyzing proton images of non-stochastic mag-

of the Thomson-scattering probe beam. We were therefore unable to measure \bar{n}_e or Δn_e for times $\gtrsim 30$ ns using the Thomson-scattering diagnostic. A reasonable estimate of \bar{n}_e can still be obtained, however, using the X-ray framing camera diagnostic. More specifically, assuming that the X-ray emission from the plasma is dominated by bremsstrahlung, we can estimate the mean electron number density $\bar{n}_e(t_1)$ at time t_1 in terms of the mean electron number density $\bar{n}_e(t_2)$ at time t_2 via the following relationship: $\bar{n}_e(t_1) \approx \bar{n}_e(t_2) [\bar{I}(t_1) / \bar{I}(t_2)]^{1/2}$,

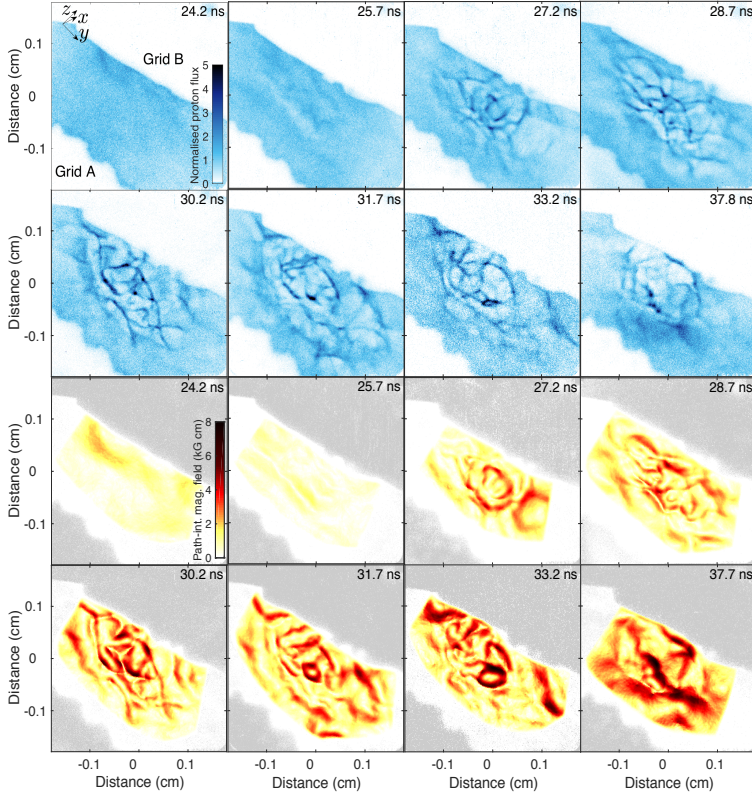


Fig. 6. 15.0 MeV proton images of interaction-region plasma, and extracted path-integrated magnetic fields. The top two rows show the proton images. Each image is approximately 300×300 pixels, with an effective pixel size of $12 \mu\text{m}$; by comparison, the proton-source size is $\sim 40 \mu\text{m}$. To prevent confusion, all images are presented with the magnification removed. The grid outline evident on the bottom left of each image is grid A, and the top-right grid is grid B. The mean proton flux Ψ_0 per pixel in these images is ~ 50 protons per pixel. The bottom two rows show the magnitude of the path-integrated perpendicular magnetic field, extracted using the field-reconstruction algorithm. The method for applying the field-reconstruction algorithm is as follows. We first select a region of the proton image to analyze; this region is chosen to be as large as possible, within the requirements of staying inside the region of high detected proton flux between the grids, maintaining an approximately rectangular shape, and choosing a boundary that does not intersect regions with high proton flux. We then embed the cropped region of proton flux inside a larger rectangular region, whose size is chosen to be as small as possible while still containing the former region. Values of proton flux are then systematically assigned to pixels outside the cropped region: these values are calculated by linearly interpolating between the nearest actual pixel value and the mean flux of the cropped region of protons. The resulting image is then subjected to a Gaussian high-pass filter, with scale 0.1 cm . This image is then processed with the field-reconstruction algorithm. Subsequent to convergence of the algorithm, the path-integrated field is only retained for pixels inside the original cropped region, with other values removed via a Gaussian window function. These steps are all necessary in order to prevent systemic errors affecting the algorithm (48).

427 netic fields (50) and consider parameterized models of known
 428 three-dimensional magnetic-field structures. To motivate a
 429 relevant model for our experimental data, we invoke the ex-
 430 pected physical origin of the early-time magnetic fields in the
 431 interaction-region plasma: the action of the Biermann battery
 432 during the interaction of the drive-beam lasers with the tar-
 433 get’s foils. This process generates azimuthal magnetic fields in
 434 the plane perpendicular to the target’s line of centers that are
 435 opposite in sign for the two foils (51). These fields are then
 436 advected by the two counter-propagating plasma flows towards
 437 the midpoint between the two foils. We therefore consider two
 438 ‘cocoon’ structures with magnetic fields of opposite sign, with
 439 their symmetry axis parallel to the line of centers.

440 A simple parameterized model for a double-cocoon configu-
 441 ration considered in (52) takes the form

$$442 \quad \mathbf{B} = \sqrt{2e} \left[B_{\text{max}}^+ e^{-\frac{(z+\ell_c)^2}{b^2}} + B_{\text{max}}^- e^{-\frac{(z-\ell_c)^2}{b^2}} \right] \frac{r}{a} e^{-\frac{r^2}{a^2}} \mathbf{e}_\phi, \quad [3]$$

443 where (r, ϕ, z) is a cylindrical coordinate system with symme-
 444 try axis z , B_{max}^+ is the maximum magnetic-field strength of
 445 the cocoon centered at $z = -\ell_c < 0$, B_{max}^- is the maximum
 446 magnetic-field strength of the cocoon centered at $z = \ell_c > 0$,
 447 a the characteristic perpendicular size of both cocoons, b their
 448 characteristic parallel size, and \mathbf{e}_ϕ the azimuthal unit vector.
 449 It can be shown (see Supplementary Information) that, if
 450 $a \gtrsim b$, then the path-integrated magnetic field associated with
 451 the double-cocoon configuration, when viewed at the $\theta = 55^\circ$
 452 angle with respect to its symmetry axis, as was done in our
 453 experiment (see Materials and Methods), is orientated predom-
 454 inantly perpendicularly to the direction of the line of centers
 455 projected onto the proton image, and its strength varies pre-

456 dominantly in the parallel direction (viz., the path-integrated
 457 field is quasi 1D). Both of these findings are consistent with the
 458 observed structure at the point of maximum path-integrated
 459 field (see Fig. 7b), validating our choice of model.

460 Having obtained a quasi-1D model for the path-integrated
 461 magnetic field (which has four free parameters: $B_{\text{max}}^+ b$, $B_{\text{max}}^- b$,
 462 a and ℓ_c – see Supplementary Information), we compare it
 463 with a lineout across the strongest path-integrated magnetic-
 464 field structure (see Fig. 7b). Fig. 7c shows the lineout, as well
 465 as the model with an optimized fit: $B_{\text{max}}^+ b = -0.31 \pm 0.02 \text{ kG cm}$,
 466 $B_{\text{max}}^- b = 0.20 \pm 0.02 \text{ kG cm}$, $a = 270 \pm 19 \mu\text{m}$, and
 467 $\ell_c = 131 \pm 9 \mu\text{m}$ (here the errors in the model parameters
 468 correspond to the 95% confidence intervals). The agreement
 469 of the model with these parameters is reasonable, with an
 470 adjusted R-squared value of 0.97. Further validation is pro-
 471 vided in the Supplementary Information (Fig. S9). The
 472 parameterized magnetic-field model itself has an additional
 473 free parameter b to be determined; this is done by assuming
 474 that the entire magnetic-field configuration is contained inside
 475 the interaction-region plasma, and so $b = \ell_n/2 \approx 0.01 \text{ cm}$. The
 476 double-cocoon configuration for this choice of b is shown in
 477 Fig. 7d. The mean magnetic-field strength associated with the
 478 double-cocoon configuration can then be shown to be $\sim 6 \text{ kG}$.
 479 This magnetic-field structure and its strength are reproduced
 480 successfully by FLASH simulations, although significant small-
 481 scale fields are also seen in the simulations that were not
 482 detected experimentally (see Fig. S11).

483 For the stochastic path-integrated magnetic fields that
 484 emerge after the jet collision (due to the interaction of the
 485 initial seed fields with stochastic fluid motions), a different
 486 approach is required: we assume statistically isotropic, ho-
 487 mogeneous, tangled magnetic fields in the interaction-region

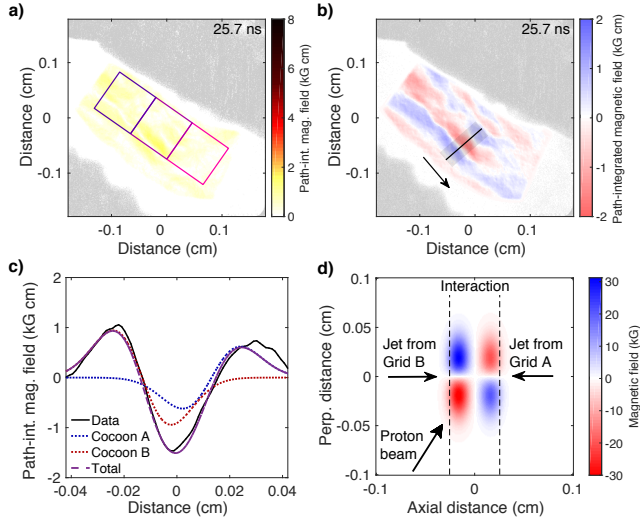


Fig. 7. Path-integrated magnetic fields at the moment of the interaction-region plasma's coalescence. **a)** Magnitude of path-integrated perpendicular magnetic field 25.7 ns after drive-beam pulse initiation. The three square regions in which the average path-integrated field is evaluated have an edge length of $800 \mu\text{m}$, and are orientated at 35° to the horizontal axis of the path-integrated field map. The center of the middle square region corresponds to the center of the proton image. **b)** Component of the path-integrated magnetic field in the direction perpendicular to the projected line of centers. This component is calculated from the full 2D perpendicular path-integrated magnetic field. The arrow indicates the (positive) direction of the chosen path-integrated field component. **c)** 1D lineout of the path-integrated field component given in **b)** (black, solid line) calculated by averaging across its width the semi-transparent rectangular region denoted in **a)**. The path-integrated field associated with model Eq. [3] is also plotted, using optimized parameters $B_{\text{max}}^+ b = -0.31 \text{ kG cm}$, $B_{\text{max}}^- b = 0.20 \text{ kG cm}$, $a = 270 \mu\text{m}$, and $l_c = 131 \mu\text{m}$. The total contribution is plotted (purple, dashed), as well as the individual contributions from the cocoons nearer grid A (blue, dotted), and nearer grid B (red, dotted). **d)** Slice plot (in the plane of basis vectors \hat{y} and \hat{z}) of B_x component associated with 3D double-cocoon magnetic-field model given by Eq. [3], with the same model parameters as shown in **c)**, and $b = 0.01 \text{ cm}$. The width of the plotted interaction region is obtained from the X-ray image recorded at the equivalent time (cf. Fig. 2c).

plasma (an assumption verified in Fig. S10), which in turn allows for the unique extraction of the RMS magnetic field strength B_{rms} via the following formula:

$$B_{\text{rms}}^2 = \frac{2}{\pi l_p} \int dk k E_{\text{path}}(k), \quad [4]$$

where l_p is the path length of the protons through the interaction region, $E_{\text{path}}(k)$ is the 1D spectrum of a given of path-integrated field under normalization condition $\int dk E_{\text{path}}(k) = (\int d^2x B_{\perp})_{\text{rms}}^2$ (48). We estimate l_p at a given time using our measurements of the average interaction-region width l_n derived from the X-ray imaging diagnostic, combined with the known angle $\theta_p \approx 55^\circ$ of the proton beam through the interaction region with respect to the line of centers (see Materials and Methods): it follows that $l_p \approx l_n / \cos \theta_p \approx 1.7l_n$. We can then calculate the characteristic correlation length ℓ_B of the stochastic magnetic field via

$$\ell_B = \frac{1}{l_p B_{\text{rms}}^2} \int dk E_{\text{path}}(k) \quad [5]$$

and determine the complete magnetic-energy spectrum $E_B(k)$ from $E_{\text{path}}(k)$ via

$$E_B(k) = \frac{1}{4\pi^2 \ell_p} k E_{\text{path}}(k). \quad [6]$$

However, we caution that due to the likely presence of strong, small-scale magnetic fields leading to self-intersection of the imaging beam, the power spectrum at wavenumbers $k \gtrsim \pi \ell_B^{-1}$ determined via Eq. [6] is not a faithful representation of the true magnetic-energy spectrum (48). We therefore focus on measuring B_{rms} and ℓ_B . We consider the three fixed regions of the path-integrated magnetic field images introduced in Fig. 7a, and calculate B_{rms} and ℓ_B for those regions.

The mean values of B_{rms} and ℓ_B arising from each path-integrated field image (and the errors on those measurements) for the full time-sequence of path-integrated field images (see Fig. 6) are shown in Fig. 8a. B_{rms} jumps significantly in a 1.5-ns interval subsequent to collision, reaching a peak value $\sim 120 \text{ kG}$, before decaying somewhat, to around $\sim 70 \text{ kG}$. The correlation length has characteristic value $\ell_B \approx 0.01 \text{ cm}$ for all measured times, except at 38 ns. The FLASH simulations, which give similar values for the magnetic-field strength, give

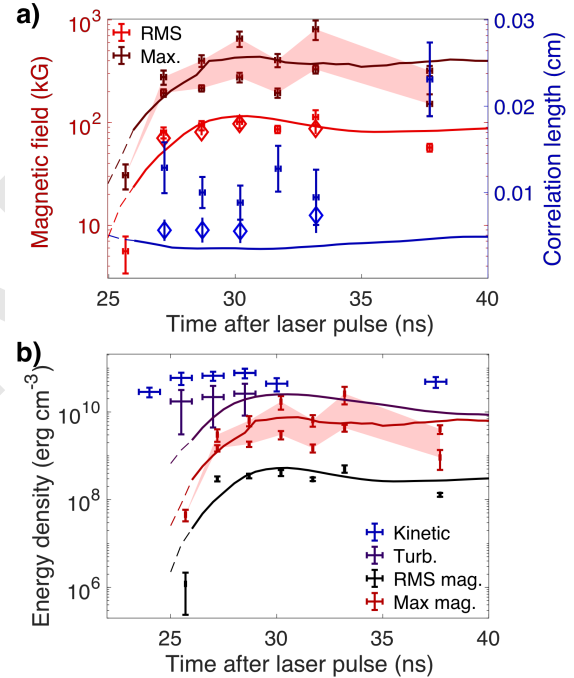


Fig. 8. Magnetic fields subsequent to formation of the interaction-region plasma. **a)** RMS magnetic-field strength (red data points) and the bounds on the maximum magnetic field (maroon band bounded by maroon data points) versus time, as well as the correlation length ℓ_B (blue data points). We emphasize that the mean and maximum field strengths at 25.7 ns are calculated differently than at the other times, on account of the non-stochastic field structure (see Fig. 7). Also shown are the evolution of the RMS magnetic field (red curve), maximum magnetic field (maroon curve) and correlation length (blue curve) versus time given by FLASH simulations of the experiment. The dashed portions of these curves correspond to times when the plasma in the interaction region is not yet fully collisional and therefore the simulations are not formally valid (see Supplementary Information). In addition, the RMS magnetic field and correlation length determined from simulated proton images of the FLASH simulations are shown as blue/red diamonds (see Fig. S26 of the Supplementary Information). **b)** Evolution of energy densities in the plasma-interaction region versus time. For times $\leq 30 \text{ ns}$, the bulk and turbulent kinetic energy densities are calculated using the values of the plasma state variables derived from the Thomson-scattering diagnostic; at later times, the plasma density required to calculate these energies is determined using the X-ray imaging diagnostic. Also shown are the evolution of the RMS magnetic energy (black curve), maximum magnetic energy (red curve) and turbulent kinetic energy (purple curve) versus time for the FLASH simulations. The dashed portions of these curves have the same meaning as in **b)**. In both **a)** and **b)**, the experimental values are shown as time intervals with vertical error bars.

524 a smaller value for the correlation length ($\ell_B \approx 0.004$ cm), a
525 discrepancy discussed in Interpretation of Results.

526 We can also calculate reasonable upper and lower bounds of
527 the maximum magnetic-field strength realized in the stochas-
528 tic field, via two different methods. For the lower bound,
529 we note that the kurtosis of the path-integrated magnetic
530 field will always be smaller than the kurtosis of the ac-
531 tual magnetic field. Therefore, the ratio between the max-
532 imum path-integrated field and the RMS path-integrated
533 field will always be smaller than the equivalent ratio for
534 the magnetic field: in other words, a reasonable lower
535 bound is $B_{\max,l} = B_{\text{rms}}(\int d^2\mathbf{x} \mathbf{B}_\perp)_{\max}/(\int d^2\mathbf{x} \mathbf{B}_\perp)_{\text{rms}}$. The
536 upper bound is derived by assuming that the maximum
537 measured path-integrated magnetic field is obtained when
538 the imaging protons cross just a single magnetic structure:
539 $B_{\max,u} = (\int d^2\mathbf{x} \mathbf{B}_\perp)_{\max}/\ell_B$. These bounds are shown in
540 Fig. 8a. At the time corresponding to maximal B_{rms} , we find
541 $310 \text{ kG} < B_{\max} < 810 \text{ kG}$.

542 Interpretation of Results

543 We conclude that our experimental platform does produce
544 a plasma that manifests stochastic motion across a range of
545 scales. In spite of some uncertainty about the late-time phys-
546 ical properties of the turbulent plasma, there exists a 4-ns
547 time interval that starts from the formation of the interaction
548 region and during which the plasma state can be thoroughly
549 characterized by our experimental diagnostics. In this interval,
550 we find that the plasma is fairly well described as classical
551 and collisional ($\lambda_e \approx 10 \mu\text{m}$, $\lambda_{CC} \approx 0.6 \mu\text{m}$, $\lambda_{HC} \approx 16 \mu\text{m}$,
552 where λ_e , λ_{CC} , and λ_{HC} are the electron, carbon-carbon and
553 hydrogen-carbon mean free paths respectively), so its transport
554 coefficients can be estimated (see Supplementary Information)
555 using collisional transport theory (53–55). Momentum trans-
556 port in the plasma is dominated by hydrogen ions, on account
557 of their long mean free path compared to carbon ions (56, 57),
558 while heat transport is dominated by electrons.

559 The time history of the fluid Reynolds number $\text{Re}_{\text{in}} =$
560 $\bar{u}_{\text{in}}L/\nu$ and the magnetic Reynolds number $\text{Rm}_{\text{in}} = \bar{u}_{\text{in}}L/\eta$ in
561 our experiment (which are defined here using the inflow velocity
562 \bar{u}_{in} in order to enable comparisons between the state of the
563 plasma both before and after the two plasma flows collide to
564 form the interaction-region plasma) is shown in Fig. 5f. Prior
565 to the collision of the plasma flows, $\text{Re}_{\text{in}} = (1.2 \pm 0.6) \times 10^3$,
566 which exceeds $\text{Rm}_{\text{in}} = 210 \pm 60$. However, after the formation
567 of the interaction-region plasma, the rapid collisional shock
568 heating of both ions and electrons simultaneously decreases the
569 resistivity and enhances the viscosity, leading to the opposite
570 ordering of dimensionless numbers: $\text{Re}_{\text{in}} = 280 \pm 180$ and
571 $\text{Rm}_{\text{in}} = 890 \pm 220$, so $\text{Pm} = \text{Rm}_{\text{in}}/\text{Re}_{\text{in}} = 3.1 \pm 2.0$. The
572 characteristic velocity u_{rms} of stochastic motions is smaller
573 than the in-flow velocity, and thus the fluid Reynolds number
574 $\text{Re} = u_{\text{rms}}L/\nu$ and magnetic Reynolds number $\text{Rm} = u_{\text{rms}}L/\eta$
575 of the driving-scale stochastic motions are somewhat smaller
576 than Re_{in} and Rm_{in} : $\text{Re} = 150 \pm 110$ and $\text{Rm} \approx 450 \pm 220$.
577 We observe that at such Re , turbulence is not ‘fully developed’
578 in the asymptotic sense. However, this is not necessary for
579 the fluctuation dynamo to operate: the fluid motions need
580 only be stochastic (19). Pm remains order unity for $t \lesssim 30$ ns;
581 since the turnover time τ_L of the largest stochastic motions
582 is $\tau_L = L/u_{\text{rms}} \approx 4$ ns, we conclude that the experimental
583 platform does indeed produce a region of plasma with $\text{Pm} \gtrsim 1$,

584 which survives longer than the timescale on which the largest-
585 scale stochastic motions decorrelate.

586 We have measured the magnetic field’s evolution with time
587 in the interaction-region plasma, and found that field strengths
588 are amplified tenfold from their initial values during the 4-ns
589 time window after collision. Having measured both the mag-
590 netic field and dynamical properties of the interaction-region
591 plasma, we can compare the time history of the turbulent and
592 magnetic energy densities (see Fig. 8b). When the interaction-
593 region plasma initially coalesces, the turbulent kinetic en-
594 ergy density $\varepsilon_{\text{turb}} \equiv \rho u_{\text{rms}}^2/2 = (1.7 \pm 1.4) \times 10^{10} \text{ erg/cm}^3$ is
595 many orders of magnitude larger than the average magnetic-
596 energy density associated with seed Biermann fields [$\varepsilon_B =$
597 $B^2/8\pi = (1.2 \pm 1.0) \times 10^6 \text{ erg/cm}^3$], implying that the latter
598 is not dynamically significant. However, 1.5 ns later, the rela-
599 tive magnitude of the magnetic energy is significantly larger:
600 $\varepsilon_B/\varepsilon_{\text{turb}} = 0.015 \pm 0.012$. Furthermore, the FLASH simula-
601 tions of our experiment – which successfully reproduce the
602 evolution of hydrodynamic variables and exhibit dynamo ac-
603 tion that results in similar energy ratios – indicate that the
604 magnetic field at the end of the 4-ns time window is dynam-
605 ically significant in at least some locations in the plasma (see
606 Fig. S21). We therefore claim to have demonstrated the
607 operation of a fluctuation dynamo in a $\text{Pm} \gtrsim 1$ plasma.

608 We can use the experimental data to infer the exponential
609 growth rate γ that would be consistent with the observed
610 evolution of the magnetic-field strength. Noting its value both
611 at collision ($B_{t=25.7 \text{ ns}} \approx 6 \text{ kG}$) and 1.5 ns later ($B_{t=27.2 \text{ ns}} \approx$
612 86 kG), we find $\gamma \gtrsim 6.7 \log(B_{t=27.2 \text{ ns}}/B_{t=25.7 \text{ ns}}) \times 10^8 \text{ s}^{-1} =$
613 $(1.8 \pm 0.4) \times 10^9 \text{ s}^{-1} \approx 4\text{--}12 u_{\text{rms}}/L$. This growth is more effi-
614 cient than that predicted by periodic-box MHD simulations
615 of the $\text{Pm} \approx 1$ fluctuation dynamo with similar parameters,
616 in which $\gamma \approx 0.3\text{--}2 u_{\text{rms}}/L$ (20, 21, 24, 25). We attribute this
617 discrepancy to strong shear flows in the interaction-region
618 plasma, directed parallel to the line of centers, in addition
619 to stochastic motions. While a 2D uni-directional shear flow
620 cannot account for sustained amplification of magnetic fields,
621 its coupling to other stochastic plasma motions (including
622 KH-unstable modes associated with the shear flow) can enable
623 dynamo action. On account of our approach for diagnosing
624 turbulence via side-on X-ray imaging of the interaction-region
625 plasma, we do not have a direct experimental measurement of
626 these shear flows; such a measurement might be possible in
627 future experiments utilizing alternative diagnostic approaches.
628 However, the FLASH simulations – which show exponential
629 growth of the field at a similar rate to that inferred from the
630 experimental data – support this interpretation (see Supple-
631 mentary Information): the RMS rate of strain of the simulated
632 velocity field, which follows the growth rate of the magnetic
633 energy, is comparable to the rate of strain of the directed
634 shear flows. Shear flows are common in astrophysical plasmas,
635 so enhanced magnetic-field amplification on account of their
636 interaction with turbulence may be relevant to astrophysical
637 systems such as galaxy clusters (58).

638 Another noteworthy finding of our experiments is the
639 characteristic scale of the amplified stochastic magnetic
640 fields, which is a factor of $\sim 2\text{--}3$ times larger than is mea-
641 sured in periodic-box MHD simulations. The integral scale
642 $L_{\text{int,B}} \equiv 4\ell_B$ of the magnetic fields that we measure is
643 the same as the driving scale L of the stochastic motions:
644 $L_{\text{int,B}} = 400 \pm 80 \mu\text{m} \approx 0.6\text{--}1.4L$; the comparable value in the

645 saturated state of periodic-box MHD simulations is robustly
646 found to be $L_{\text{int,B}} \approx 0.3L$ at similar Rm and Pm (22, 25).
647 The characteristic value of the integral scale obtained directly
648 from the FLASH simulations of our experiment, in which the
649 magnetic-energy spectrum evolves similarly in time to the
650 previous periodic-box simulations (see Supplementary Infor-
651 mation, Fig. S22), is also smaller than the experimentally
652 measured value. Part of this apparent discrepancy is an arti-
653 fact of technical issues that can inhibit accurate determination
654 of the high-wavenumber tail of the magnetic-energy spectrum
655 from proton-imaging data (see Fig. S23). Extracting path-
656 integrated field maps from simulated proton images of the
657 FLASH simulations and subsequently inferring the correlation
658 length using the same approach applied to the experimental
659 data, we find closer agreement (see Fig. 8a, blue diamonds),
660 which suggests a possible overestimation of the correlation
661 lengths attained experimentally. Yet some discrepancy in the
662 inferred correlation length remains, particularly at early times.
663 The robustness of this discrepancy is confirmed by direct anal-
664 ysis of simulated proton images of the FLASH simulations
665 (Fig. S24), or the magnetic-energy spectra inferred from both
666 experimental and simulated path-integrated field maps (Fig.
667 S25). This result is tantalizing, given the long-standing prob-
668 lem of explaining the observed scale of tangled magnetic fields
669 present in the ICM (59): current ICM simulations tend to
670 predict magnetic fields at smaller scales than observed (60, 61).

671 A simple possible explanation for why the characteristic
672 scale of the magnetic fields in the FLASH simulations is smaller
673 at early times than in our experiment arises from the presence
674 of small-scale seed magnetic fields in the latter just after the
675 jet collision that are not observed experimentally (see Section
676 C). We attribute this difference to the fact that the results of
677 a one-fluid MHD code such as FLASH are not a valid model of
678 the interaction region before collisional thermalization between
679 the two jets has occurred (which, as we show in the Supple-
680 mentary Information, takes place by $t \approx 26.5$ ns). Recent
681 work (62) shows that the magnetic-energy spectrum and the
682 correlation length associated with the dynamo-amplified fields
683 are time-dependent functions of the initial spectrum of seed
684 fields for the degree of magnetic-energy amplification we real-
685 ize in our experiment. Thus the small-scale seed fields present
686 in the FLASH simulations but not in the experimental data
687 could cause the correlation length in the FLASH simulations
688 to be smaller than in the experiment for a period post collision.
689 Other possible explanations include additional physical pro-
690 cesses that could arise due to the order-unity Hall parameter
691 being attained subsequent to the seed field's amplification (63),
692 or differences in the mechanism of resistive dissipation between
693 the experiments and the simulations enabling a more efficient
694 inverse magnetic-energy cascade in the former (64).

695 Finally, we note that the maximum measured ratio of ε_B to
696 $\varepsilon_{\text{turb}}$ – at $t \approx 28.7$ ns, which is also the latest time at which such
697 a measurement was successfully made in the experiment – is
698 $\varepsilon_B/\varepsilon_{\text{turb}} = 0.03 \pm 0.02$. This value, which is also obtained (but
699 not surpassed, even at later times) in the FLASH simulations,
700 is a factor of a few smaller than that obtained for $\text{Pm} \approx 1$ MHD
701 simulation at saturation with comparable Reynolds numbers
702 ($\varepsilon_B/\varepsilon_{\text{turb}} \approx 0.08$) (25). There are two possible explanations
703 for the lower measured values of $\varepsilon_B/\varepsilon_{\text{turb}}$ in the experiment.
704 First, the time at which this measurement is taken is less than
705 a single driving-scale eddy turnover time after the turbulent

696 plasma is formed; thus, it is likely that insufficient time has
697 passed for the saturated state of the fluctuation dynamo to be
698 obtained in the experiment. Second, due to conductive losses,
699 the plasma cools significantly for times $\gtrsim 30$ ns, attaining
700 characteristic temperatures $T_e \approx T_i \approx 80$ eV at $t = 37.5$ ns (in
701 the absence of heating by the Thomson-scattering probe beam
702 – see Supplementary Information). Since both $\text{Rm} \propto T_e^{3/2}$ and
703 $\text{Pm} \propto T_e^{3/2} T_i^{5/2}$ are sensitive functions of temperature, this
704 cooling results in a transition to a different parameter regime:
705 $\text{Rm} \approx 20$, and $\text{Pm} \approx 10^{-3}$. This transition should inhibit
706 dynamo action, although to our knowledge, such a transition
707 occurring during the nonlinear phase of the fluctuation dynamo
708 has not been studied previously.

709 In summary, our experiment supports the notion that turbu-
710 lent plasma with $\text{Pm} \gtrsim 1$ and sufficiently large Rm is capable
711 of amplifying magnetic fields up to dynamical strengths. Fur-
712 thermore, the time-resolved characterization provided by the
713 experiment has demonstrated that magnetic-field amplifica-
714 tion in the plasma occurs at a much larger rate than the
715 stretching rate associated with the outer scale of the turbu-
716 lent motions. This rate of growth is greater than is typically
717 obtained in periodic-box MHD simulations with equivalent
718 Mach number, Rm, and Pm, a finding that we attribute to
719 the presence of strong directed shears in the interaction-region
720 plasma. The characteristic scale of these fields is found to be
721 larger than anticipated by resistive-MHD simulations, includ-
722 ing our MHD FLASH simulations of the experiment, which
723 otherwise faithfully reproduce the plasma's evolution. Both
724 findings suggest that the fluctuation dynamo – when operating
725 in realistic plasma – may be capable of generating large-scale
726 magnetic fields more efficiently than currently expected by
727 analytic theory or MHD simulations.

728 Materials and Methods

729 **X-ray framing camera specifications.** Images of self-emitted soft X-
730 rays from the interaction-region plasma were recorded using a fram-
731 ing camera (65, 66) configured with a two-strip microchannel plate
732 (MCP) (67) and a $50 \mu\text{m}$ pinhole array. The pinhole array was
733 situated 9.14 cm away from the center of the target and the main
734 detector at 27.4 cm, giving rise to a $\times 2$ image magnification. A thin
735 filter composed of $0.5 \mu\text{m}$ polypropylene and 150 nm of aluminum was
736 placed in front of the MCP, removing radiation with photon energy
737 $\lesssim 100$ eV. The MCP itself was operated with a 1 ns pulse-forming
738 module at a constant 400 V bias, and the two strips sequentially
739 gated: this allowed for two images (time-integrated over a 1 ns
740 interval) of the plasma at pre-specified times to be detected for
741 each experimental shot. Electrons exiting the MCP struck a phos-
742 phor plate, producing an optical image, which was recorded using
743 a 4096×4096 $9\text{-}\mu\text{m}$ pixel charge-coupled-device (CCD) camera.
744 The chosen voltage bias was such that the response of the CCD
745 camera was linear and thus the relative counts of two given pixels
746 provided a measure of the relative (optical) intensity incident on
747 the CCD. To allow comparison between the X-ray images of the
748 interaction-region plasma at different stages of its evolution, the
749 framing-camera bias was fixed throughout the experiment and its
750 value optimized for probing the interaction-region plasma at peak
751 emission. Given this normalization and the measured signal-to-
752 noise ratio, the effective dynamic range of the camera was ~ 100 .
753 The frequency-response curves of various components of the X-ray
754 framing camera, along with the combined response, are shown in
755 Fig. S1a of the Supplementary Information.

756 **Thomson-scattering diagnostic specifications.** The Thomson-
757 scattering diagnostic employed a 30 J, frequency-doubled (526.5
758 nm) laser, which probed the plasma in a cylindrical volume with
759 cross-sectional area $50 \mu\text{m}^2$ and length 1.5 mm centered on the
760

770 target's center, which coincided with the target-chamber centre
 771 (TCC). The orientation of the scattering volume is shown in Fig.
 772 1. The scattered light was collected at scattering angle 63° . As
 773 mentioned in Experimental Design, the Thomson-scattering signal
 774 was resolved spatially along the cylindrical scattering volume and
 775 integrated over the 1 ns duration of the laser pulse. The high-
 776 and low-frequency components of the spectrum were recorded
 777 separately using two distinct spectrometers; the separation was
 778 performed using a beam splitter.

779 **Thomson-scattering data analysis.** To interpret the IAW and EPW
 780 features, a theory relating the scattered laser light detected at a
 781 particular wavelength – or, equivalently, frequency – to fundamental
 782 properties of the plasma is needed. For a given scattering vector
 783 \mathbf{k} , it can be shown (68) that the spectrum $I(\mathbf{k}, \omega)$ of the laser light
 784 scattered by the plasma at frequency ω is given by

$$785 \quad I(\mathbf{k}, \omega) = N_e I_0 \sigma_T S(\mathbf{k}, \omega), \quad [7]$$

786 where N is the total number of scattering electrons, I_0 the intensity
 787 of the incident laser, $\sigma_T \equiv (q_e^2/m_e c)^2 \sin^2 \vartheta_T$ the Thomson cross-
 788 section for scattering by a free electron (q_e is the elementary charge,
 789 m_e the electron mass, c the speed of light, and ϑ_T the angle between
 790 the direction of the electric field of the incident and scattered light),
 791 and

$$792 \quad S(\mathbf{k}, \omega) \equiv \frac{1}{2\pi N_e} \int dt \exp[i(\omega - \omega_0)t] \langle n_e(\mathbf{k}, 0) n_e(\mathbf{k}, t)^* \rangle \quad [8]$$

793 is the dynamic form factor (ω_0 being the frequency of the incident
 794 light). Assuming that the distribution functions of the electrons
 795 and ions are close to shifted Maxwellian distributions, with electron
 796 number density n_e , electron temperature T_e , temperature T_j of
 797 ion species j , and bulk fluid velocity \mathbf{u} , and also that the Debye
 798 length is $\lambda_D \lesssim 10^{-6}$ cm (assumptions justified by Table S2 of the
 799 Supplementary Information), we find that $\alpha \equiv 1/k\lambda_D \gtrsim 8 > 1$;
 800 thus, we can employ the Salpeter approximation for the dynamic
 801 form factor (68):

$$802 \quad S(\mathbf{k}, \omega) \approx \frac{1}{k v_{the}} \Gamma_\alpha \left(\frac{\tilde{\omega} - \omega_0}{k v_{the}} \right) \\ 803 \quad + \sum_j \frac{Z_j}{k v_{thj}} \left(\frac{\alpha^2}{1 + \alpha^2} \right)^2 \Gamma_{\bar{\alpha}_j} \left(\frac{\tilde{\omega} - \omega_0}{k v_{thj}} \right), \quad [9]$$

804 where $\tilde{\omega} \equiv \omega - \mathbf{k} \cdot \mathbf{u}$ is the Doppler-shifted frequency, the sum is
 805 over all ion species in the plasma, Z_j is the charge of ion species j ,

$$806 \quad \Gamma_\alpha(x) \equiv \frac{\exp(-x^2)}{\sqrt{\pi} |1 + \alpha^2 [1 + xZ(x)]|^2}, \quad [10]$$

807 and $\bar{\alpha}_j = Z_j \alpha^2 T_e / T_j (1 + \alpha^2)$. The complex function $Z(x)$ is the
 808 plasma dispersion function (69). For low-frequency fluctuations
 809 (in particular, ion-acoustic waves), $\omega - \omega_0 \sim k v_{thj}$ and so the
 810 first term on the right-hand side of [9] is small by a factor of
 811 $\mathcal{O}[Z_i(m_e T_i)^{1/2} / (m_i T_e)^{1/2}] \ll 1$ when compared to the second (this
 812 factor is indeed small provided the ion temperature T_i – assumed
 813 equal for all ion species – is comparable to the electron temperature);
 814 thus the shape of the low-frequency spectrum is dominated by the
 815 second term. For high-frequency fluctuations (electron plasma
 816 waves) satisfying $\omega - \omega_0 \sim k v_{the}$, the second term is smaller than
 817 the first by an exponential factor $\mathcal{O}[\exp(-m_e T_i / m_i T_e)] \ll 1$; thus
 818 the shape of the high-frequency spectrum is dominated by the first
 819 term. We conclude that we can relate physical properties of the
 820 plasma to the measured EPW and IAW features using fits given by
 821 the first and second terms of [9], respectively.

822 However, for our experiment, there is a complication: the pres-
 823 ence of stochastic motions and density fluctuations. The presence of
 824 such fluctuations means that the bulk fluid velocity \mathbf{u} and electron
 825 density n_e are not necessarily fixed parameters inside the Thomson-
 826 scattering volume during the time-integrated measurement, but
 827 instead possess a range of values. To account for this range, we
 828 assume that fluctuations of velocity and density are isotropic and
 829 normally distributed, with means $\bar{\mathbf{u}}$ and \bar{n}_e , and standard deviations
 830 Δu and Δn_e , respectively. Under this assumption, the appropriate

fit for the IAW feature is

$$831 \quad S_{IAW}(\mathbf{k}, \omega) \approx \frac{\sqrt{3}}{\sqrt{\pi} \Delta u} \int d\tilde{u}_\parallel \exp \left[-\frac{3(\tilde{u}_\parallel - \bar{u}_\parallel)^2}{\Delta u^2} \right] \\ 832 \quad \times \sum_j \frac{Z_j}{k v_{thj}} \frac{\alpha^4}{(1 + \alpha^2)^2} \Gamma_{\bar{\alpha}_j} \left(\frac{\omega - k \bar{u}_\parallel - \omega_0}{k v_{thj}} \right), \quad [11] \quad 833$$

where $\bar{u}_\parallel \equiv \hat{\mathbf{k}} \cdot \mathbf{u}$. For the EPW feature, we use

$$834 \quad S_{EPW}(\mathbf{k}, \omega) \approx \frac{1}{\sqrt{\pi} \Delta n_e} \int d\tilde{n}_e \exp \left[-\frac{(\tilde{n}_e - \bar{n}_e)^2}{\Delta n_e^2} \right] \\ 835 \quad \times \frac{1}{k v_{the}} \Gamma_\alpha \left(\frac{\omega - \omega_0}{k v_{the}} \right). \quad [12] \quad 836$$

837 In spite of the seeming complexity of these equations, for a fully
 838 ionized CH plasma the spectral shapes implied by [11] and [12] are
 839 quite simple: a double peak structure, where the position and width
 840 of the peaks depend on plasma parameters. For the IAW feature,
 841 the distance between the peaks provides a measure of T_e ; the shift
 842 in the position of the double-peaked spectrum with respect to the
 843 incident probe beam's frequency gives a measurement of the bulk
 844 velocity \bar{u}_\parallel ; the width of both peaks is a function of both T_i and of
 845 the small-scale stochastic velocity dispersion Δu . The effect of the
 846 density on the shape of the IAW feature is negligible. For the EPW
 847 feature, the opposite holds: the position of the peak is determined
 848 by n_e . The width of the peak is in general determined by a range
 849 of factors – Landau damping, collisions and the range of fluctuating
 850 densities Δn_e . For our experiment, both collisional broadening and
 851 that by Landau damping are small (because $k\lambda_e \gg 1$ and $\alpha^2 \gg 1$,
 852 respectively), but the spread of densities can be significant. The
 853 fitting procedure is described in the Supplementary Information.

854 **Proton-imaging diagnostic specifications.** The proton imaging diag-
 855 nostic was implemented by imploding a D^3He capsule (70): the
 856 capsule (diameter $420 \mu\text{m}$) is composed of $2 \mu\text{m}$ of SiO_2 (coated
 857 with aluminum), and filled with 18 atm D^3He gas (6 atm D_2 and
 858 12 atm 3He). The capsule is imploded using 17, 270 J beams, each
 859 with a 600 ps pulse length, and 1.82 mm defocus. This results in
 860 the generation of $\sim 10^9$ 3.3 MeV and 15.0 MeV protons via nuclear
 861 fusion reactions. These protons rapidly travel outward from the cen-
 862 ter of the backlighter as a uniform spherical sheet, passing through
 863 the plasma-filled volume, before reaching a detector composed of
 864 interleaved metal sheets and solid-state nuclear track detector, CR-
 865 39 (71) (chemical formula $C_{12}H_{18}O_7$). The specific design of the
 866 detector is as follows: 7.5 μm of tantalum, then 1.5 mm of CR-39,
 867 then 150 μm of aluminum, and finally another 1.5 mm of CR-39.
 868 This design ensures that 3.3 MeV protons are stopped in the first
 869 layer of CR-39, and 15.0 MeV protons in the second; the tantalum
 870 filter minimizes damage to the CR-39 resulting from X-rays. Highly
 871 charged ions deposit the majority of their energy close to where they
 872 are stopped completely, leaving small tracks of broken molecular
 873 bonds. The positions of these tracks is determined by etching the
 874 CR-39 for two to three hours in a 6N solution of sodium hydroxide,
 875 yielding tracks with diameters $\sim 10 \mu\text{m}$. An automated microscope
 876 system records the location of tracks, before removing image defects
 877 and counting the number of protons in preset bin sizes: the output
 878 are proton (fluence) images. The robust design of the detector is
 879 such that protons reaching the detector are recorded with close
 880 to 100% efficiency. The dimensions of the imaging set-up are as
 881 follows: the distance r_i from the proton source to the center of the
 882 target is $r_i = 1$ cm, and the distance from the proton source to the
 883 detector is 28 cm. The magnification of the imaging set-up is thus
 884 $\times 28$. The geometry of the target is such that the line connecting
 885 the center of the proton source to the target's geometric center is at
 886 an angle $\theta_p = 55^\circ$ to the z axis. On account of the comparatively
 887 large distance of the proton source from the target's center ($r_i = 1$
 888 cm) compared to the transverse extent of the interaction-region
 889 plasma ($l_{n\perp} \lesssim 0.3$ cm), which is centered on the target's geometric
 890 center, the deviation of the angle of any imaging proton passing
 891 through the interaction region with respect to θ_p is $\lesssim 6^\circ$.

892 **ACKNOWLEDGMENTS.** The research leading to these results
 893 has received funding from the European Research Council under the

894 European Community's Seventh Framework Programme (FP7/2007-
895 2013)/ERC grant agreements no. 256973 and 247039, the U.S.
896 Department of Energy (DOE) National Nuclear Security Adminis-
897 tration (NNSA) under Contract No. B591485 to Lawrence Liver-
898 more National Laboratory (LLNL), Field Work Proposal No. 57789
899 to Argonne National Laboratory (ANL), Subcontract No. 536203
900 with Los Alamos National Laboratory, Subcontract B632670 with
901 LLNL, and grants No. DE-NA0002724, DE-NA0003605, and DE-
902 NA0003934 to the University of Chicago, DE-NA0003868 to the
903 Massachusetts Institute of Technology, and Cooperative Agreement
904 DE-NA0003856 to the Laboratory for Laser Energetics Univer-
905 sity of Rochester. We acknowledge support from the U.S. DOE
906 Office of Science Fusion Energy Sciences under grant No. DE-
907 SC0016566 and the National Science Foundation under grants No.
908 PHY-1619573, PHY-2033925, and AST-1908551. Awards of com-
909 puter time were provided by the U.S. DOE ASCR Leadership
910 Computing Challenge (ALCC) program, using resources at ANL,
911 which is supported by the U.S. DOE Office of Science under contract
912 No. DE-AC02-06CH11357. We acknowledge funding from grants
913 2016R1A5A1013277 and 2017R1A2A1A05071429 of the National
914 Research Foundation of Korea. Support from AWE plc., the En-
915 gineering and Physical Sciences Research Council (grant numbers
916 EP/M022331/1, EP/N014472/1, and EP/R034737/1) and the U.K.
917 Science and Technology Facilities Council is also acknowledged.

- 918 1. R Beck, Magnetic fields in spiral galaxies, *Astron. Astrophys. Rev.* **24**, 1 (2015)
- 919 2. V Vacca *et al.* Magnetic fields in galaxy clusters and in the large-scale structure of the uni-
920 verse, *Galaxies* **6**, 142 (2018)
- 921 3. L Biermann, and A Schluter, Cosmic radiation and cosmic magnetic fields. II. Origin of cosmic
922 magnetic fields, *Phys. Rev.* **29**, 29 (1951)
- 923 4. RM Kulsrud, R Cen, JP Ostriker and D Ryu, The protogalactic origin for cosmic magnetic
924 fields, *Astrophys. J.* **480**, 481 (1997)
- 925 5. R Kulsrud, A critical review of galactic dynamos, *Annu. Rev. Astron. Astrophys.* **37**, 37 (1999)
- 926 6. K Subramanian, From primordial seed magnetic fields to the galactic dynamo, *Galaxies* **7**, 47
927 (2019)
- 928 7. K Subramanian, A Shukurov, and NEL Haugen, Evolving turbulence and magnetic fields in
929 galaxy clusters, *Mon. Not. R. Astron. Soc.* **366**, 1437 (2006)
- 930 8. D Ryu, H Kang, J Cho, and S Das, Turbulence and magnetic fields in the large-scale structure
931 of the universe, *Science* **320**, 909 (2008)
- 932 9. GK Batchelor, On the spontaneous magnetic field in a conducting liquid in turbulent motion,
933 *Proc. R. Soc. A.* **201**, 405 (1950)
- 934 10. F Rincon, Dynamo theories, *J. Plasma Phys.* **85**, 205850401 (2019)
- 935 11. AP Kazentsev, Enhancement of a magnetic field by a conducting fluid, *Soviet-JETP* **26**, 1031
936 (1968)
- 937 12. SI Vainstein, and YB Zel'dovich, Review of topical problems: origin of magnetic fields in
938 astrophysics (turbulent 'dynamo' mechanisms), *Sov. Phys. Usp.* **15**, 159 (1972)
- 939 13. YB Zel'dovich, AA Ruzmaikin, SA Molchanov, and DD Sololov, Kinematic dynamo problem in
940 a linear velocity field, *J. Fluid Mech.* **144**, 1 (1984)
- 941 14. R Kulsrud, and SW Anderson, The spectrum of random magnetic fields in the mean field
942 dynamo theory of the galactic magnetic field, *Astrophys. J.* **396**, 606 (1992)
- 943 15. M Meneguzzi, U Frisch, and A Pouquet, Helical and nonhelical turbulent dynamos, *Phys. Rev.*
944 *Letts.* **47**, 1060 (1981)
- 945 16. S Kida, S Yanase, and J Mizushima, Statistical properties of MHD turbulence and turbulent
946 dynamo, *Phys. Fluids A*, **3**, 457 (1991)
- 947 17. RS Miller, F Mashayek, V Adumitroaie, and P Givi, Structure of homogeneous nonhelical
948 magnetohydrodynamic turbulence, *Phys. Plasmas* **3**, 3304 (1996)
- 949 18. J Cho, and ET Vishniac, The generation of magnetic fields through driven turbulence, *Astro-*
950 *phys. J.* **538**, 217 (2001)
- 951 19. AA Schekochihin, SC Cowley, SF Taylor, JL Maron, and JC McWilliams, Simulations of the
952 small-scale turbulent dynamo, *Astrophys. J.* **612**, 276 (2004)
- 953 20. NE Haugen, A Brandenburg, and W Dobler, Simulations of nonhelical hydromagnetic turbu-
954 lence, *Phys. Rev. E* **70**, 016308 (2004)
- 955 21. AA Schekochihin, AB Isakov, SC Cowley, JC McWilliams, MRE Proctor and TA Yousef, Fluc-
956 tuation dynamo and turbulent induction at low magnetic Prandtl numbers, *New J. Phys.* **9**,
957 300 (2007)
- 958 22. J Cho, and D Ryu, Characteristic lengths of magnetic field in magnetohydrodynamic turbu-
959 lence, *Astrophys. J.* **705**, L90 (2009)
- 960 23. A Beresnyak, Universal nonlinear small-scale dynamo, *Phys. Rev. Lett.* **108**, 035002 (2012)
- 961 24. DH Porter, TW Jones, and D Ryu Vorticity, shocks, and magnetic fields in subsonic, ICM-like
962 turbulence gas motions in the intra-cluster medium, *Astrophys. J.* **810**, 93 (2015)
- 963 25. A Seta, PJ Bushby, A Shukurov and TS Wood, On the saturation mechanism of the fluctuation
964 dynamo at $Pm > 1$, *Phys. Rev. Fluids* **5**, 043702 (2020)
- 965 26. AA Ruzmaikin, and DD Sokolov, The magnetic field in mirror-invariant turbulence, *Sov. Astron.*
966 *Letts.* **7**, 388 (1981)
- 967 27. S Boldyrev, and F Cattaneo, Magnetic-field generation in Kolmogorov turbulence, *Phys. Rev.*
968 *Letts.* **92**, 144501 (2004)
- 969 28. AB Isakov, AA Schekochihin, SC Cowley, JC McWilliams, and MRE Proctor Numerical
970 demonstration of fluctuation dynamo at low magnetic Prandtl numbers, *Phys. Rev. Lett.* **98**,
971 208501 (2007)
- 972 29. C Federrath, J Schober, S Bovino, and DRG Schleicher, The turbulent dynamo in highly
973 compressible supersonic plasmas *Astrophys. J. Letts.* **797**, L19 (2014)
30. J Cho, ET Vishniac, A Beresnyak, A Lazarian, and D Ryu, Growth of magnetic fields induced
974 by turbulent motions, *Astrophys. J.* **693**, 1449 (2009)
- 975 31. NE Haugen, A Brandenburg, and W Dobler, Is nonhelical hydromagnetic turbulence peaked
976 at small scales?, *Astrophys. J.* **597**, L141 (2003)
- 977 32. G Gregori *et al.*, Generation of scaled protogalactic seed magnetic fields in laser-produced
978 shock waves, *Nature* **481**, 480 (2012)
- 979 33. J Meinecke *et al.*, Turbulent amplification of magnetic fields in laboratory laser-produced
980 shock waves, *Nat. Phys.* **10**, 520 (2014)
- 981 34. J Meinecke *et al.*, Developed turbulence and nonlinear amplification of magnetic fields in
982 laboratory and astrophysical plasmas, *Proc. Nat. Acad. Sci.* **112**, 8211 (2015)
- 983 35. G Gregori, B Reville, and F Miniati The generation and amplification of intergalactic mag-
984 netic fields in analogue laboratory experiments with high power lasers, *Phys. Reports.* **601**, 1
985 (2015)
- 986 36. P Tzeferacos *et al.*, Numerical modeling of laser-driven experiments aiming to demonstrate
987 magnetic field amplification via turbulent dynamo *Phys. Plasmas* **24**, 041404 (2017)
- 988 37. P Tzeferacos *et al.*, Laboratory evidence of dynamo amplification of magnetic fields in a
989 turbulent plasma *Nat. Commun.* **9**, 591 (2018)
- 990 38. T Boehly *et al.*, Initial performance results of the OMEGA laser system, *Optics Communica-*
991 *tions* **133**, 495 (1997)
- 992 39. B Fryxell *et al.*, FLASH: An Adaptive Mesh Hydrodynamics Code for Modeling Astrophysical
993 Thermonuclear Flashes, *Astrophys. J.* **131**, S273 (2000)
- 994 40. P Tzeferacos *et al.*, FLASH MHD simulations of experiments that study shock generated
995 magnetic fields., *High Energy Dens. Phys.* **17**, 24 (2015)
- 996 41. S Müller *et al.*, Evolution of the design and fabrication of astrophysics targets for turbulent
997 dynamo (TDYNO) experiments on OMEGA *Fusion Sci. Tech.* **73**, 434 (2017)
- 998 42. A Rigby, J Katz, AFA Bott, TG White, P Tzeferacos, DQ Lamb, DH Froula, G Gregori. Imple-
999 mentation of a Faraday rotation diagnostic at the OMEGA laser facility, *High Power Laser*
1000 *Science and Engineering* **6** (2018)
- 1001 43. GB Rybicki and AP Lightman, Radiative processes in astrophysics. (Wiley-VCH, Weinheim,
1002 2004)
- 1003 44. E Churazov *et al.*, X-ray surface brightness and gas density fluctuations in the Coma cluster,
1004 *Mon. Not. R. Astron. Soc.* **421**, 1123 (2012)
- 1005 45. I Zhuravleva *et al.*, The relation between gas density and velocity power spectra in galaxy
1006 clusters: qualitative treatment and cosmological simulations, *Astrophys. J.* **788**, L13 (2014)
- 1007 46. TG White *et al.*, Supersonic plasma turbulence in the laboratory, *Nature Comm.* **10**, 1758
1008 (2019)
- 1009 47. NL Kugland *et al.*, Relation between electric and magnetic field structures and their proton-
1010 beam images, *Rev. Sci. Instrum.* **83**, 101301 (2012)
- 1011 48. AFA Bott, C Graziani, TG White, P Tzeferacos, DQ Lamb, G Gregori, and AA Schekochihin
1012 Proton imaging of stochastic magnetic fields, *J. Plasma Phys.* **83**, 6 (2017)
- 1013 49. W Ganbgo, and RJ McCann The geometry of optimal transportation, *Acta Math.* **177**, 113-
1014 161 (1996)
- 1015 50. G Sarri *et al.*, Dynamics of self-generated, large amplitude magnetic fields following high-
1016 intensity laser matter interaction, *Phys. Rev. Lett.* **109**, 205002. (2012)
- 1017 51. JA Stamper *et al.*, Spontaneous magnetic Fields in laser-produced plasmas, *Phys. Rev. Lett.*
1018 **26**, 1012 (1971)
- 1019 52. NL Kugland *et al.*, Visualizing electromagnetic fields in laser-produced counter-streaming
1020 plasma experiments for collisionless shock laboratory astrophysics, *Phys. Plasmas* **20**,
1021 056313 (2013)
- 1022 53. SI Braginskii, Transport processes in a plasma, in: M.A. Leontovich (Ed.), Reviews of Plasma
1023 Physics, vol. 1. (1965), p. 205.
- 1024 54. JD Huba, NRL plasma formulary. (Naval Research Laboratory, Washington DC, 1994)
- 1025 55. DD Ryutov, RP Drake, and J Kane, Similarity criteria for the laboratory simulation of super-
1026 nova hydrodynamics, *Astrophys. J.* **518**, 821 (1999)
- 1027 56. AN Simakov and K Molvig, Electron transport in a collisional plasma with multiple ion species,
1028 *Phys. Plasmas* **21**, 024503 (2014)
- 1029 57. AN Simakov and K Molvig, Hydrodynamic description of an unmagnetized plasma with mul-
1030 tiple ion species. II. Two and three ion species plasmas. *Phys. Plasmas* **23**, 032116 (2016)
- 1031 58. A Simionescu *et al.*, Constraining gas motions in the intra-cluster medium. *Space Sci. Rev.*
1032 **215**, 24 (2019)
- 1033 59. AA Schekochihin, and SC Cowley Turbulence, magnetic fields, and plasma physics in clusters
1034 of galaxies, *Phys. Plas.* **13**, 056501 (2006)
- 1035 60. S Roh, D Ryu, H Kang, S Ha1, and H Jang, Turbulence dynamo in the stratified medium of
1036 galaxy clusters *Astrophys. J.* **883**, 138 (2019)
- 1037 61. F Vazza, G Brunetti, M Bruggen, and A Bonafede, Resolved magnetic dynamo action in the
1038 simulated intracluster medium *Mon. Not. R. Astron. Soc.* **472**, 1672 (2018)
- 1039 62. A Seta, and C Federrath, Seed magnetic fields in turbulent small-scale dynamos, *Mon. Not.*
1040 *R. Astron. Soc.* **499**, 2076 (2020)
- 1041 63. MG Haines, Magnetic-field generation in laser fusion and hot-electron transport *Can. J. Phys.*
1042 **64**, 86 (1986)
- 1043 64. AA Schekochihin, MHD turbulence: a biased review. arXiv:2010.00699 (01 October 2020)
- 1044 65. JD Kilkenny, P Bell, R Hanks, G Power, RE Turner, and J Wiedwald, High-speed gated x-ray
1045 imagers. *Rev. Sci. Instrum.* **59**, 1793 (1988)
- 1046 66. DK Bradley, PM Bell, OL Landen, JD Kilkenny and J Oertel, Development and characteriza-
1047 tion of a pair of 30–40 ps x-ray framing cameras. *Rev. Sci. Instrum.* **66**, 716 (1995)
- 1048 67. GA Rochau *et al.*, Energy dependent sensitivity of microchannel plate detectors. *Rev. Sci.*
1049 *Instrum.* **802**, 323 (2006)
- 1050 68. DE Evans and J Katzenstein, Laser light scattering in laboratory plasmas. *Rep. Prog. Phys.*
1051 **32**, 207 (1969).
- 1052 69. BD Fried and SD Conte, The plasma dispersion function. (Academic Press, New York, 1961)
- 1053 70. C. Li *et al.*, Measuring E and B Fields in laser-produced plasmas with monoenergetic proton
1054 radiography, *Phys. Rev. Lett.* **97**, 3 (2006)
- 1055 71. FH Séguin *et al.*, Spectrometry of charged particles from inertial-confinement-fusion plas-
1056 mas. *Rev. Sci. Instrum.* **74**, 975 (2003)
- 1057